Bridging hcp-Ni and Ni$_3$C via a Ni$_3$C$_{1-x}$ Solid Solution: Tunable Composition and Magnetism in Colloidal Nickel Carbide Nanoparticles

Zachary L. Schaefer,[†] Kaitlyn M. Weeber,[†] Rajiv Misra,[‡,§] Peter Schiffer,[‡,§] and Raymond E. Schaak*[,†,§]

[†]Department of Chemistry, [‡]Department of Physics, and [§]Materials Research Institute, The Pennsylvania State University, University Park, Pennsylvania 16802, United States

Ⓢ *Supporting Information*

ABSTRACT: Nanoparticles of elemental nickel underpin a large number of magnetic and catalytic applications, and the possibility of tuning these properties via the formation of different allotropes is intriguing. While bulk elemental nickel adopts a face centered cubic (fcc) structure, a growing number of reports suggest that colloidal nickel nanoparticles can crystallize in the metastable hexagonal close packed (hcp) structure. However, there is some disagreement in the literature concerning the formation of hcp-Ni, particularly with respect to the crystallographically-related Ni$_3$C phase. Most notable is a

range of lattice constants and magnetic properties that have been attributed to hcp-Ni. Here, we show that reaction time can be used to tune the carbon content of a Ni$_3$C$_{1-x}$ solid solution. Importantly, colloidal nanoparticles of Ni$_3$C$_{1-x}$ can help to experimentally rationalize the range of lattice constants and magnetic properties reported for hcp-Ni and Ni$_3$C, effectively bridging these two end-member systems. All samples, including those isolated immediately upon reduction of Ni^{2+} to Ni^0, contained some carbon, as evidenced by XRD, XPS, TGA, DSC, TEM, and SQUID magnetometry. As reaction time increases, the average carbon content increases, and this correlates with a systematic increase in unit cell volume and a systematic decrease in saturation magnetization. These results also provide a straightforward pathway for tuning the magnetic properties of isomorphous Ni nanoparticles.

KEYWORDS: magnetic nanoparticles, nickel, nickel carbide, composition-tunable solid solution

■ INTRODUCTION

Nanoparticles of elemental nickel have been widely studied because of their important magnetic[1,2] and catalytic properties.[3,4] Bulk elemental nickel typically adopts the face centered cubic (fcc) structure, but hexagonal close packed (hcp) and body centered cubic (bcc) allotropes have also been examined both theoretically[5−8] and experimentally.[9−13] Nanoparticles of fcc-Ni are common; many reports have described colloidal routes to fcc-Ni with a range of sizes and morphologies.[1,14−18] A series of recent reports have suggested that colloidal nanoparticles of the metastable hcp-Ni allotrope are also accessible using the polyol process and other reactions carried out in high-boiling organic solvents.[19−28]

There is, however, some disagreement in the literature concerning the formation of colloidal hcp-Ni nanoparticles.[29,30] First, the phase claimed to be the metastable hcp-Ni allotrope is generally formed at higher temperatures than the stable fcc-Ni phase,[19,20,23−26] which is counterintuitive. Second, carbon has been experimentally observed in colloidal nanoparticles synthesized using protocols similar to those that are reported to generate hcp-Ni.[29,31] Third, the powder X-ray diffraction (XRD) pattern for hcp-Ni differs only subtly from that of Ni$_3$C, which is structurally similar (Figure 1). Ni$_3$C is

rhombohedral and forms an ordered superstructure of interstitial carbon in an hcp-Ni lattice, but its structure can be approximated by a hexagonal subcell that is nearly identical in size to that of hcp-Ni (Figure 1).[32] Indeed, the reported lattice constants for colloidal hcp-Ni ($a = 2.65−2.67$ Å, $c = 4.33−4.35$ Å) match better with the hexagonal subcell of Ni$_3$C ($a = 2.6449$ Å, $c = 4.3296$ Å)[33] than with pure hcp-Ni ($a = 2.622$ Å, $c = 4.321$ Å).[9] Fourth, the reported saturation magnetization (M_s) values for colloidally synthesized hcp-Ni nanoparticles are significantly smaller than those for analogous fcc-Ni nanoparticles with similar sizes and morphologies, with some reports suggesting that colloidal hcp-Ni nanoparticles are actually nonmagnetic.[19] Overall, the M_s values for hcp-Ni nanoparticles are observed to be much smaller than expected. Importantly, pure hcp-Ni is predicted to be highly magnetic with saturation magnetization values similar to that of fcc-Ni,[5−8] while Ni$_3$C is nominally nonmagnetic, although small regions with substoichiometric interstitial carbon could still maintain a very small magnetic moment.[34]
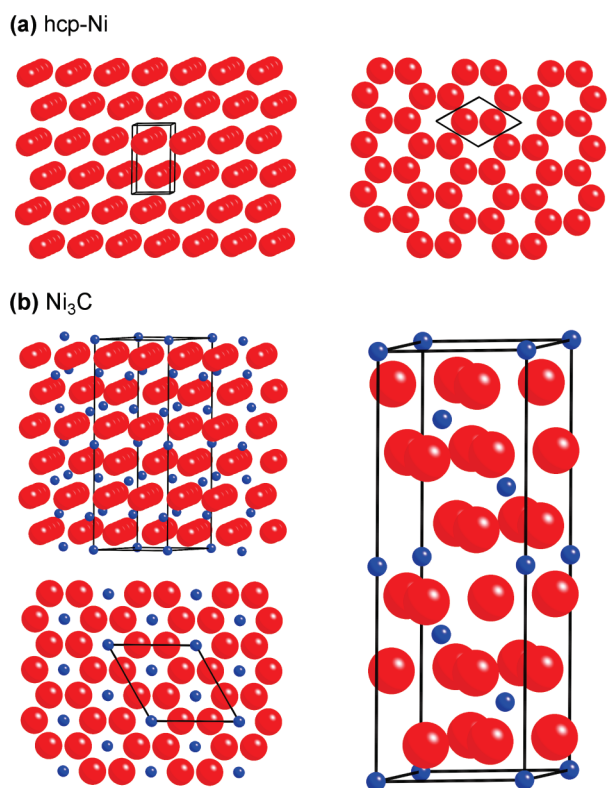
(a) hcp-Ni

(b) Ni₃C

Figure 1. Crystal structures of (a) hexagonal hcp-Ni and (b) rhombohedral Ni_3C,[35] highlighting the similarities between the structures and the location of the interstitial carbon in Ni_3C. Nickel atoms are represented by large red spheres, and carbon atoms are represented by small blue spheres. The unit cell of Ni_3C in (b) shows the superlattice structure.

In this report, we show that a series of Ni_3C_{1-x} nanoparticles can help to experimentally rationalize the discrepancies in lattice constants and magnetic properties that have been previously reported for hcp-Ni. We use a synthetic protocol that is closely related to existing colloidal routes that have yielded particles attributed to both hcp-Ni and Ni_3C. Our data show that reaction time can be used to tune average carbon content via a continuous Ni_3C_{1-x} solid solution, and these samples effectively bridge prior reports of hcp-Ni and Ni_3C. All samples contain some carbon, and as carbon content increases, the unit cell volume increases and the M_S values decrease.

■ EXPERIMENTAL SECTION

Synthesis of Ni_3C_{1-x}. Nickel 2,4-pentanedionate (204 mg, 95%, Alfa-Aesar) was added to a 100-mL three-neck round-bottomed flask. Subsequently, 1-octadecene (5 mL, 90%, Alfa-Aesar) and oleylamine (5 mL, 70% technical grade, Aldrich) were added along with a magnetic stir bar and the flask was fitted with a thermometer, condenser, and septum. The flask was then heated using a mantle to 120 °C at a rate of ~5 °C/min while periodically evacuating and backfilling with Ar. The solution was then heated at the same rate to ~215 °C, at which point the solution became black. We consider samples isolated at this point to have a dwell time (t) of <2 min because of the length of time over which the solution becomes black and the difficulty in establishing an absolute point at which $t = 0$ min. Samples can be isolated at different dwell times by holding the temperature constant at ~215 °C. After the desired time is reached, the sample is removed from the mantle and
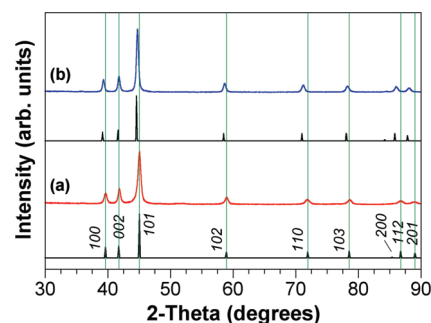

Figure 2. Powder XRD data for (a) the earliest-isolated sample with a dwell time (t) of <2 min at ~215 °C (red) and (b) the sample isolated after t = 1 h (blue). Simulated XRD patterns (black) in (a) and (b) correspond to hcp-Ni and Ni_3C, respectively.[35] The vertical lines correlate with the peak positions of hcp-Ni.

allowed to cool to room temperature (within approximately 5 min) and then collected by centrifugation with a large excess of acetone. The precipitate is then dispersed in hexanes and collected by centrifugation with a large excess of acetone. This washing process is performed three times after which the particles are allowed to dry under ambient conditions. This isolation and washing procedure generally produces approximately 35 mg of product.

Characterization. Powder X-ray diffraction (XRD) patterns were collected at room temperature using a Bruker-AXS D8 Advance diffractometer with a LynxEye 1-D detector using Cu Kα radiation. Lattice parameters were refined with the Le Bail method[36] using the Topas software package.[37] Transmission electron microscopy (TEM) and selected area electron diffraction (SAED) were performed using a JEOL 1200 EX-II operating at an accelerating voltage of 80 kV. Magnetic characterization was performed using a Quantum Design superconducting quantum interference device (SQUID) magnetometer with an accessible temperature range of 1.8−800 K and magnetic fields up to 7 T. The samples were loaded in a gelatin capsule for measurements up to 350 K. For higher temperature measurements, the sample was loaded inside a roll of aluminum foil. Thermogravimetric analysis (TGA) and differential scanning calorimetry (DSC) were performed simultaneously using a TA Instruments SDT Q600 with alumina crucibles, ~5 mg of sample, and a heating rate of 10 °C/min under a 100 mL/min flow of argon. X-ray photoelectron spectroscopy (XPS) was performed using a monochromatic Al Kα source instrument (Kratos, Axis Ultra, England) operating at 14 kV and 20 mA. Spectra were collected with a pass energy of 20 eV, and the binding energies were calibrated by referencing the most intense C 1s peak to contaminant carbon (285 eV).

■ RESULTS AND DISCUSSION

Most existing colloidal routes to hcp-Ni[19−28] and Ni_3C[29,38,39] nanoparticles involve the reduction of soluble Ni^{2+} salts in glycol or alkylamine solvents by heating to temperatures of 180−320 °C in the presence of molecular or polymeric surface stabilizers, with the identity of the solvent influencing the temperature at which carbon is incorporated.[39] Our protocol is consistent with these literature reports, which (by analogy to known chemistry) are capable of generating an active carbon species via thermal and metal-catalyzed solvent decomposition.[40,41] Specifically, our Ni_3C_{1-x} nanoparticles were prepared by dissolving $Ni(acac)_2$ in octadecene and oleylamine and heating to ~215 °C. This temperature is within the range of temperatures previously reported to yield Ni_3C.[29,38,39] Samples with different average carbon contents were accessed by holding
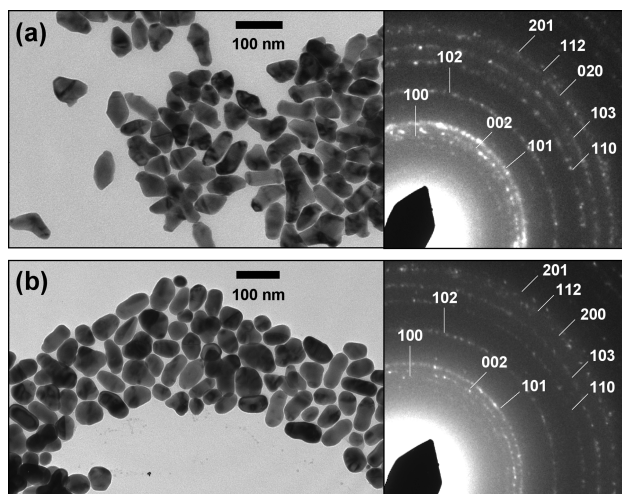
Figure 3. TEM images and SAED patterns for (a) the sample with $t < 2$ min at $\sim$215 °C and (b) the sample isolated at $t = 1$ h. The indexing on the SAED patterns corresponds to a hexagonal cell.

Figure 4. Powder XRD data for the five isolated aliquots, as described in the text. The bottom pattern (black) shows the earliest-isolated sample with $t < 2$ min at $\sim$215 °C and the top pattern (red) shows the sample isolated after $t = 1$ h. The insets show expanded regions to better highlight the trends in peak shifts. Indexing in the top inset corresponds to a hexagonal cell, and the vertical lines indicate the (100) peak positions for Ni_3C and hcp-Ni, based on literature values.[33,9]

the reaction at $\sim$215 °C for different dwell times, which generally ranged from approximately 1 to 60 min.

Figure 2 shows powder XRD data for a sample isolated at a very early stage of the reaction, e.g., with a dwell time (t) at $\sim$215 °C of less than 2 min, as well as a sample isolated after $t = 1$ h. The sample corresponding to $t < 2$ min (which will be discussed in more detail later and reclassified as a rhombohedral Ni_3C_{1-x} phase) has refined hexagonal lattice constants of $a = 2.6292(2)$ Å and $c = 4.3223(4)$ Å. These values match well with those reported previously for evaporated films of hcp-Ni ($a = 2.622$ Å and $c = 4.321$ Å), which appear to be the most reliable lattice constants for pure hcp-Ni because of the remote possibility of carbon contamination during the reduced-pressure deposition process.[9] The sample for which $t = 1$ h (which will also be discussed in more detail later and reclassified as a rhombohedral Ni_3C_{1-x} phase) has refined hexagonal lattice constants of $a = 2.651(1)$ Å and $c = 4.3306(2)$ Å, which match well with a prior report of colloidal Ni_3C ($a = 2.65$ Å and $c = 4.34$ Å)[29] and an earlier report on fully carburized bulk nickel ($a = 2.6449$ Å and $c = 4.3296$ Å).[33] However, the lattice constant values we obtain for the 1-h sample, which match well with those of Ni_3C, are often attributed in the literature to colloidal nanoparticles of hcp-Ni because of comparison with XRD patterns in the Powder Diffraction File (PDF) database, which contains several entries that do not likely correspond to pure hcp-Ni free of interstitial carbon, boron, or nitrogen.

Figure 3 shows representative TEM images and SAED patterns for the two samples described above. Most of the particles are elongated with multiple facets, having average dimensions of 90 nm (length) × 45 nm (width). Importantly, there is no statistically significant difference in the morphologies and sizes of the samples; both exhibit variations in morphology and size, and these variations are highly similar across all samples. As a rough measure of this, the average nanoparticle areas are 2072 ± 698 nm^2 for the $t < 2$ min sample and 2556 ± 980 nm^2 for the $t = 1$ h sample. These values statistically overlap, and coupled with the TEM images in Figure 3, this indicates that the average morphology and size dispersity do not change significantly as heating time increases, so these factors are assumed to be constant among samples and therefore are not likely to
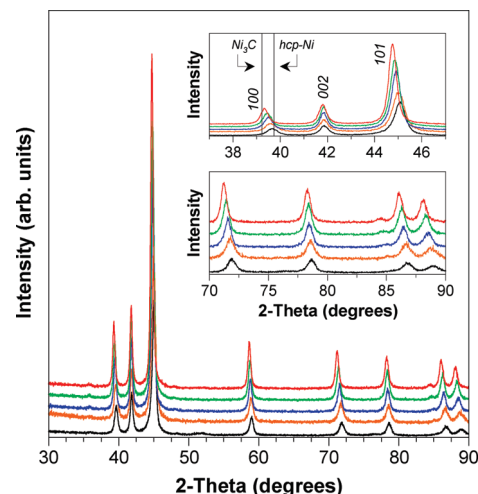
significantly influence the observed properties. The SAED patterns for the two samples are similar as well, with the most intense rings being characteristic of a hexagonal lattice. Scherrer analysis of XRD peak broadening indicates domain sizes that range from 30 to 45 nm, which suggests that the particles are largely polycrystalline with multiple domains; this is consistent with the irregular morphologies of the particles.

In addition to these two "end member" samples isolated after short and long dwell times, aliquots taken as the reaction progresses allow us to isolate other members of the Ni_3C_{1-x} solid solution. Powder XRD data (Figure 4) show the end members from Figure 2 along with three additional intermediate samples isolated after $t = 2$, 10, and 20 min. Carbon is likely incorporated at different rates in particles of different sizes (given the distribution of size and morphology evident in Figure 3). However, all samples exhibit highly symmetric peaks, with no evidence of the asymmetry that often characterizes solid solutions with significant compositional variation. The progressive shift of peak positions toward lower angles as reaction time increases is clearly evident, particularly in the expanded regions shown as insets. This is consistent with the expansion of the unit cell as more interstitial carbon is incorporated as a function of reaction time. Interestingly, the top inset to Figure 4 shows that the (100) and (101) reflections shift to lower angles while the (002) reflections remain more constant. This indicates that the lattice expansion is anisotropic, occurring primarily in the $a-b$ plane. Similar structural anisotropy has been previously noted in solution-synthesized nickel boride nanoparticles.[42] The refined hexagonal lattice constants, collected in Table S1, reflect this trend as well. (Note that the $t = 2$ min "intermediate" sample and the $t < 2$ min "end member" sample were isolated at nearly the same time, yet have slightly different lattice constants. This highlights the almost immediate incorporation of carbon, the difficulty in potentially isolating a "pure" sample of hcp-Ni, and the impact that small variations in reaction time can have on the average composition of the product.)
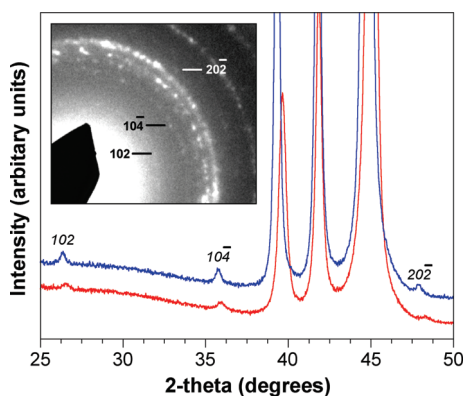
Figure 5. Powder XRD data showing higher-resolution scans of the end member samples with $t < 2$ min at $\sim$215 °C (bottom, red) and $t = 1$ h (top, blue). The superlattice reflections of rhombohedral Ni_3C are labeled and clearly evident. The inset shows an expanded view of the SAED pattern from Figure 2a, highlighting the presence of the rhombohedral superlattice peaks. Note that the superlattice peaks also shift to lower angles as more carbon is incorporated.

Figure 6. Plots of (a, b) DC magnetization (M) vs temperature at an applied field of 100 Oe and (c, d) DC magnetization (M) vs applied field (H) at 5 K for four samples of Ni_3C_{1-x} with increasing amounts of carbon as a function of dwell time at $\sim$215 °C. The samples are color coded according to dwell time (e.g., carbon content): black (<2 min), red (5 min), blue (30 min), and green (60 min). For the plots in (a) and (b), filled squares correspond to field cooled (FC) data and open squares correspond to zero field cooled (ZFC) data. Panel (d) shows an enlarged region of panel (c).

Although Ni_3C is sometimes described as hexagonal, its true structure is rhombohedral (Figure 1).[32] The hexagonal subcell can account for most of the reflections observed by powder XRD, but the rhombohedral supercell captures the longer-range ordering of the interstitial carbon that is present in bulk Ni_3C. Previous reports of colloidally synthesized Ni_3C nanoparticles have not, to our knowledge, shown data explicitly confirming the presence of a rhombohedral supercell, and some reported lattice constants refer to the hexagonal subcell. Because the rhombohedral superlattice reflections are weak, we collected powder XRD patterns of the two end member samples with long data acquisition times in order to increase the signal-to-noise ratio to a level where superlattice peaks could be observed if they are present. Figure 5 shows that both end-member samples (corresponding to samples with the minimum and maximum observed amounts of carbon) exhibit superlattice peaks attributable to the rhombohedral cell of Ni_3C. The inset to Figure 5 shows an enlargement of the SAED pattern initially presented in Figure 2a, and the superlattice peaks are also evident. Thus, we conclude that all of the Ni_3C_{1-x} samples—even those isolated at very short dwell times that have lattice parameters similar to those expected for hcp-Ni—do indeed contain carbon, and they are best described in relation to rhombohedral Ni_3C rather than hexagonal hcp-Ni. Refined rhombohedral lattice constants for all samples are collected in Table S1; both hexagonal and rhombohedral lattice constants are provided for the same samples in order to facilitate full comparison with prior reports.

Several characterization tools, in addition to our observation of the rhombohedral Ni_3C superlattice by XRD, help to confirm the presence of carbon in all samples, as well as confirm that the peak shifts observed by XRD can be correlated to average carbon content. X-ray photoelectron spectroscopy (XPS) shows evidence of interstitial carbon in both end member samples (Figure S1), consistent with prior XPS studies of colloidal Ni_3C nanoparticles.[29,38] Thermogravimetric analysis (TGA) of the Ni_3C_{1-x} samples shows weight loss below 300 °C that is attributable to desorption of surface water and decomposition of the organic surface stabilizers, as well as an additional higher-temperature weight loss in the range of 475−875 °C that we attribute to loss of carbon from the nickel carbide phase since significant
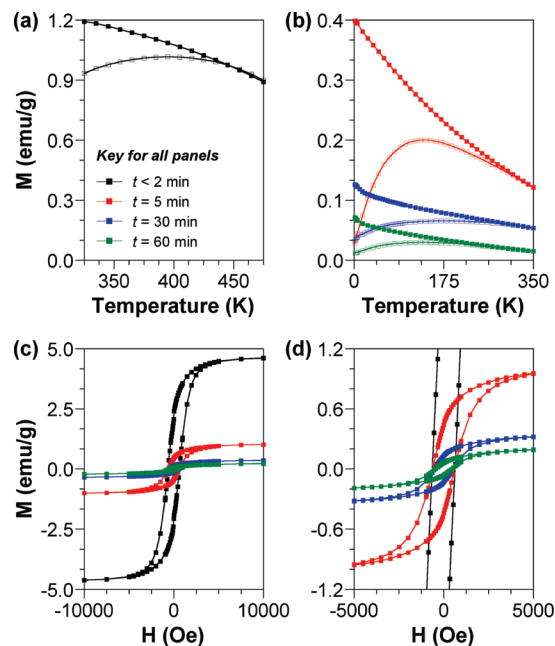
weight loss due to nickel vaporization is unlikely in this temperature range (Figure S2). This interpretation of the TGA data is also consistent with an earlier study.[43] Indeed, stoichiometric Ni_3C is known to decompose into nickel and carbon near 420 °C,[31,43] and we observe an exotherm near this temperature in all samples that is attributed to decomposition of the nickel carbide phase (Figure S2). The progressive shift of the exotherm to higher decomposition temperatures for samples heated for longer times is consistent with the trend expected for samples with increasing carbon content because of increasing nickel−carbon bonding interactions.[44] Using the weight loss above the decomposition temperature as a rough estimate of minimum average carbon content, the five samples from Figure 4 are estimated to have minimum average carbon contents that systematically increase from approximately 0.5 wt % ($x \approx 0.9$ in Ni_3C_{1-x}) for the first aliquot to approximately 4.0 wt % ($x \approx 0.4$ in Ni_3C_{1-x}) for the sample heated at $\sim$215 °C for 1 h. This is consistent with the trend in peak shifts and lattice constants observed by XRD.

The magnetic properties of several Ni_3C_{1-x} samples, shown in Figure 6 and collected in Table S2, are also consistent with the increasing incorporation of carbon as a function of reaction time. The samples in Figure 6 are different from those used in the structural analyses above because the small sample sizes isolated during those aliquot studies precluded reliable magnetic measurements. However, the Ni_3C_{1-x} samples used for magnetic measurements were made in the same way, e.g., heating at $\sim$215 °C with different dwell times that span <2 min−1 h. As expected, these particles are statistically identical in morphology,

size, and size dispersity to those shown in Figure 3. As a result, these factors are the same across all samples, and thus significant differences in magnetic properties among samples are not likely to be attributable to differences in morphology, size, or size distribution. Weight loss between 100 and 300 °C, measured by TGA analysis, indicated similar amounts of surfactant in all samples, making any differences in surfactant amounts statistically insignificant. Thus, differences in surfactant amounts among samples are not likely to contribute in a significant way to differences in weight-normalized magnetic properties.

Figure 6a shows plots of magnetization (M) vs temperature (T), including both field cooled (FC) and zero field cooled (ZFC) data, at an applied field of 100 Oe for the sample with the least amount of carbon ($t < 2$ min). Analogous plots of M vs. T for the other samples with increasing amounts of carbon ($t = 5$, 30, and 60 min) are shown in Figure 6b. The bifurcation between the FC and ZFC data suggests a superparamagnetic blocking temperature, although we cannot rule out the possibility of a spin-glass-like magnetic state, particularly for the sample with the largest average carbon content. As average carbon content increases as a function of reaction time at ~215 °C, the temperature at which the FC and ZFC curves bifurcate decreases: 445, 325, 300, and 260 K for the samples heated at ~215 °C for 2, 5, 30, and 60 min, respectively (Table S2). (We take the bifurcation temperature to be the temperature at which the FC and ZFC curves diverge by 0.001 emu/g.)

Figure 6c shows a plot of M vs applied field (H), which indicates that as the average carbon content increases, the M_s values systematically decrease from a maximum of 4.61 emu/g for the sample with the least carbon to 0.21 emu/g for the sample with the most carbon (Table S2). (The two intermediate samples have M_S values of 1.01 and 0.35 emu/g.) The coercive fields also decrease systematically (632, 604, 519, and 463 Oe) as average carbon content increases (Table S2). (The plot in Figure 6d shows an enlarged version of the plot in Figure 6c, highlighting the trends in the samples with low M_s values.) We cannot rule out the possibility that very small amounts of fcc Ni impurities are present, or that small amounts of Ni^{2+} are adsorbed to the particles' surfaces, which would contribute to the nonzero magnetization for the sample with the largest average carbon content. However, theoretical studies have shown that pure Ni_3C should be nonmagnetic due to hybridization between the carbon and nickel orbitals, and any nonzero moments that are observed in Ni_3C are attributable to structural disorder.[34] Our results are consistent with this: as average carbon content increases, M_s values decrease but do not reach zero.

Literature reports of M_s values for samples attributed to hcp-Ni are typically in the range of 0.025−11.5 emu/g,[20−28] which includes the range of M_s values observed for all of our samples. Because M_S values are typically reported in units of emu/g for the fcc-Ni, hcp-Ni, and Ni_3C systems, they can vary as a function of particle size, morphology, and amount of organic or polymeric surface stabilizer present. However, as mentioned earlier, our samples all have similar amounts of organic surface stabilizers, as well as similar morphologies, sizes, and size distributions. Thus, these factors are approximately the same across all samples, and therefore they are unlikely to significantly influence the weight-normalized magnetic properties. In contrast to the M_s values reported previously for hcp-Ni, all reported M_S values are measurably higher (e.g., 25−55 emu/g) for fcc-Ni nanoparticles synthesized as control samples in the same studies that also claim the formation of hcp-Ni (e.g., situations

where all compared samples use related synthetic protocols and have generally the same sizes, shapes, and surface stabilizers).[19,23−25,27,28]

Our samples with lattice constants that best match Ni_3C (e.g., longer reaction times) show very weak magnetism, while those that more closely match hcp-Ni (e.g., shorter reaction times, yet still contain small amounts of interstitial carbon) have an appreciable magnetic response. The direct correlation of lattice constant, average carbon content, and magnetism in this study experimentally bridges the prior reports of hcp-Ni and Ni_3C and offers a mechanism for experimentally rationalizing the widely variable magnetic properties reported for hcp-Ni.[29,30] Most synthetic protocols that have been reported to yield colloidal hcp-Ni and Ni_3C maintain a peak temperature of 180−320 °C for more than 30 min, and our data therefore imply that all of those samples likely contain some carbon and fall within the Ni_3C_{1-x} solid solution. Even the sample synthesized with a very short (<2 min) dwell time at ~215 °C, which has lattice parameters close to those expected for pure hcp-Ni and shows M_s values on par with the values typically attributed to hcp-Ni nanoparticles, contains a non-negligible amount of carbon—enough to form an observable rhombohedral superlattice and impact the observed magnetic properties.

CONCLUSIONS

In conclusion, we have shown that the tunable carbon content and magnetic properties of Ni_3C_{1-x} solid solution nanoparticles help to experimentally rationalize the range of lattice constants and M_S values previously reported for colloidal hcp-Ni and Ni_3C nanoparticles. Specifically, the average carbon content of colloidal Ni_3C_{1-x} nanoparticles can be tuned as a function of reaction time, and the lattice constants and M_S values of these Ni_3C_{1-x} solid solution nanoparticles span the range of values that are typically reported for both hcp-Ni and Ni_3C. Even the sample with the least amount of carbon, having lattice constants and M_S values close to those previously attributed to hcp-Ni, showed evidence of the rhombohedral Ni_3C superlattice. These insights help to experimentally clarify some of the discrepancies in the literature concerning colloidal hcp-Ni vs Ni_3C nanoparticles. These results also represent a straightforward pathway for tuning the magnetic properties of isomorphous Ni nanoparticles by controlling the average carbon content as a function of reaction time.

ASSOCIATED CONTENT

ⓢ Supporting Information. Additional XRD, XPS, TGA, DSC, and magnetism data. This material is available free of charge via the Internet at http://pubs.acs.org.

AUTHOR INFORMATION

Corresponding Author
*E-mail: schaak@chem.psu.edu.

ACKNOWLEDGMENT

■ REFERENCES

(1) Murray, C. B.; Sun, S. H.; Doyle, H.; Betley, T. *MRS Bull.* **2001**, *26*, 985–991.

(2) Lu, A. H.; Salabas, E.; Schüth, F. *Angew. Chem., Int. Ed.* **2007**, *46*, 1222–1244.

(3) Hofmann, S.; Sharma, R.; Ducati, C.; Du, G.; Mattevi, C.; Cepek, C.; Cantoro, M.; Pisana, S.; Parvez, A.; Cervantes-Sodi, F.; Ferrari, A. C.; Dunin-Borkowski, R.; Lizzit, S.; Petaccia, L.; Goldoni, A.; Robertson, J. *Nano Lett.* **2007**, *7*, 602–608.

(4) Metin, Ö; Mazumder, V.; Özkar, S.; Sun, S. *J. Am. Chem. Soc.* **2010**, *132*, 1468–1469.

(5) Papaconstantopoulos, D. A.; Fry, J. L.; Brener, N. E. *Phys. Rev. B* **1989**, *39*, 2526–2528.

(6) Podgórny, M.; Goniakowski, J. *Phys. Rev. B* **1990**, *42*, 6683–6693.

(7) Guo, G. Y.; Wang, H. H. *Chin. J. Phys.* **2000**, *38*, 949–961.

(8) He, X.; Kong, L. T.; Liu, B. X. *J. Appl. Phys.* **2005**, *97*, 106107.

(9) Hemenger, P.; Weik, H. *Acta Crystallogr.* **1965**, *19*, 690–691.

(10) Heinrich, B.; Arrott, A. S.; Cochran, J. F.; Liu, C.; Myrtle, K. *J. Vac. Sci. Technol., A* **1986**, *4*, 1376–1379.

(11) Tang, W. X.; Qian, D.; Wu, D.; Wu, Y. Z.; Dong, G. S.; Jin, X. F.; Chen, S. M.; Jiang, X. M.; Zhang, X. X.; Zhang, Z. *J. Magn. Magn. Mater.* **2002**, *240*, 404–406.

(12) Tian, C. S.; Qian, D.; Wu, D.; He, R. H.; Wu, Y. Z.; Tang, W. X.; Yin, L. F.; Shi, Y. S.; Dong, G. S.; Jin, X. F.; Jiang, X. M.; Liu, F. Q.; Qian, H. J.; Sun, K.; Wang, L. M.; Rossi, G.; Qiu, Z. Q.; Shi, J. *Phys. Rev. Lett.* **2005**, *94*, 137210.

(13) Tian, W.; Sun, H. P.; Pan, X. Q.; Yu, J. H.; Yeadon, M.; Boothroyd, C. B.; Feng, Y. P.; Lukaszew, R. A.; Clarke, R. *Appl. Phys. Lett.* **2005**, *86*, 131915.

(14) Cordente, N.; Respaud, M.; Senocq, F.; Casanove, M.-J.; Amiens, C.; Chaudret, B. *Nano Lett.* **2001**, *1*, 565–568.

(15) Park, J.; Kang, E.; Son, S. U.; Park, H. M.; Lee, M. K.; Kim, J.; Kim, K. W.; Noh, H. J.; Park, J. H.; Bae, C. J.; Park, J. G.; Hyeon, T. *Adv. Mater.* **2005**, *17*, 429–434.

(16) Leng, Y. H.; Zhang, Y. H.; Liu, T.; Suzuki, M.; Li, X. G. *Nanotechnology* **2006**, *17*, 1797–1800.

(17) Leng, Y.; Li, Y.; Li, X.; Takahashi, S. *J. Phys. Chem. C* **2007**, *111*, 6630–6633.

(18) Carenco, S.; Boissière, C.; Nicole, L.; Sanchez, C.; Le Floch, P.; Mézailles, N. *Chem. Mater.* **2010**, *22*, 1340–1349.

(19) Chinnasamy, C. N.; Jeyadevan, B.; Shinoda, K.; Tohji, K.; Narayanasamy, A.; Sato, K.; Hisano, S. *J. Appl. Phys.* **2005**, *97*, 10J309.

(20) Mi, Y.; Yuan, D.; Liu, Y.; Zhang, J.; Xiao, Y. *Mater. Chem. Phys.* **2005**, *89*, 359–361.

(21) Jeon, Y. T.; Moon, J. Y.; Lee, G. H.; Park, J.; Chang, Y. *J. Phys. Chem. B* **2006**, *110*, 1187–1191.

(22) Tzitzios, V.; Basina, G.; Gjoka, M.; Alexandrakis, V.; Georgakilas, V.; Niarchos, D.; Boukos, N.; Petridis, D. *Nanotechnology* **2006**, *17*, 3750–3755.

(23) Chen, Y. Z.; Peng, D. L.; Lin, D. P.; Luo, X. H. *Nanotechnology* **2007**, *18*, 505703.

(24) Han, M.; Liu, Q.; He, J. H.; Song, Y.; Xu, Z.; Zhu, J. M. *Adv. Mater.* **2007**, *19*, 1096–1100.

(25) Gong, J.; Wang, L. L.; Liu, Y.; Yang, J. H.; Zong, Z. G. *J. Alloys Compd.* **2008**, *457*, 6–9.

(26) Wang, H.; Jiao, X.; Chen, D. *J. Phys. Chem. C* **2008**, *112*, 18793–18797.

(27) Chen, Y. Z.; Luo, X. H.; She, H. D.; Yue, G. H.; Peng, D. L. *J. Nanosci. Nanotechnol.* **2009**, *9*, 5157–5163.

(28) Luo, X.; Chen, Y.; Yue, G.-H.; Peng, D.-L.; Luo, X. *J. Alloys Compd.* **2009**, *476*, 864–868.

(29) Goto, Y.; Taniguchi, K.; Omata, T.; Otsuka-Yao-Matsuo, S.; Ohashi, N.; Ueda, S.; Yoshikawa, H.; Yamashita, Y.; Oohashi, H.; Kobayashi, K. *Chem. Mater.* **2008**, *20*, 4156–4160.

(30) He, L. *J. Magn. Magn. Mater.* **2010**, *322*, 1991–1993.

(31) Schaefer, Z. L.; Gross, M. L.; Hickner, M. A.; Schaak, R. E. *Angew. Chem., Int. Ed.* **2010**, *49*, 7045–7048.

(32) Nagakura, S. *J. Phys. Soc. Jpn.* **1958**, *13*, 1005–1014.

(33) Hofer, L. J. E.; Cohn, E. M.; Peebles, W. C. *J. Phys. Colloid Chem.* **1950**, *54*, 1161–1169.

(34) Yue, L. P.; Sabiryanov, R.; Kirkpatrick, E. M.; Leslie-Pelecky, D. L. *Phys. Rev. B* **2000**, *62*, 8969–8975.

(35) Villars, P. *Pearson's Handbook: Desk ed.*, 1st ed.; ASM International: Materials Park, OH, 1997.

(36) Lebail, A.; Duroy, H.; Fourquet, J. L. *Mater. Res. Bull.* **1988**, *23*, 447–452.

(37) *TOPAS*, version 3.0; general profile and structure analysis software for powder diffraction data; Bruker AXS: Karlsruhe, Germany.

(38) Leng, Y. G.; Shao, H. Y.; Wang, Y. T.; Suzuki, M.; Li, X. G. *J. Nanosci. Nanotechnol.* **2006**, *6*, 221–226.

(39) Leng, Y. H.; Liu, Y.; Song, X. B.; Li, X. G. *J. Nanosci. Nanotechnol.* **2008**, *8*, 4477–4481.

(40) Davis, S. C.; Severson, S. J.; Klabunde, K. J. *J. Am. Chem. Soc.* **1981**, *103*, 3024–3029.

(41) Hooker, P.; Tan, B. J.; Klabunde, K. J.; Suib, S. *Chem. Mater.* **1991**, *3*, 947–952.

(42) Schaefer, Z. L.; Ke, X.; Schiffer, P.; Schaak, R. E. *J. Phys. Chem. C* **2008**, *112*, 19846–19851.

(43) Leng, Y. H.; Xie, L.; Liao, F. H.; Zheng, J.; Li, X. G. *Thermochim. Acta* **2008**, *473*, 14–18.

(44) Esconjauregui, S.; Whelan, C. M.; Maex, K. *Carbon* **2009**, *47*, 659–669.

2480

dx.doi.org/10.1021/cm200410s |*Chem. Mater.* 2011, 23, 2475–2480